Integrated Switching Circuit for Low-Noise Self-Referenced Mid-Infrared Absorption Sensing Using Silicon Waveguides

Yanli Qi, Zhexuan Zheng, Mehdi Banakar, Yangbo Wu, Anushka Gangnaik, David J. Rowe, Vinita Mittal, Jonathan Butement, James S. Wilkinson, Goran Z. Mashanovich, and Milos Nedeljkovic

***Abstract*—We report a new method of accurately measuring the mid-infrared absorption of fluid analytes using on-chip waveguides that allows measurements to be referenced for noise and drift reduction whilst using only a single external detector. A silicon-on-insulator waveguide circuit integrated with a microfluidic channel is made in which a pair of switches alternate light between an evanescent absorption sensor waveguide and a reference waveguide at a rate of a few kHz, thus allowing low frequency common noise components to be removed from the measurement, and leading to a reduction in the noise floor by a factor of 11 compared to a simple waveguide absorption sensor. The device was verified by using it to detect an Isopropyl alcohol (IPA) absorption peak at a wavelength of 3.77 μm.**

***Index Terms*—Mid-infrared, silicon photonics, optical switching, microfluidics, absorption spectroscopy.**

I. Introduction

ABSORPTION spectroscopy in the mid-infrared (MIR) wavelength region has a variety of potential applications [1] including atmospheric monitoring [2], detection of chemicals and explosives [3], human breath analysis [4], non-invasive glucose monitoring [5], and plant and crop science [6]. Absorption spectroscopy can provide unique spectra to identify substances present in a sample and can also measure their concentration [7].

There are a range of benefits to using waveguides for MIR absorption spectroscopy, such as significantly reduced dimensions, reduced fabrication costs, they could enable non-specialists to operate diagnostic tools [8]. They also offer accurately controllable light-analyte interaction, and they only require small analyte volumes. For absorption spectroscopy based on waveguides, the platform should be sensitive, re-usable, and have a wide low loss transparency range in the MIR region.

A recent demonstration of on-chip sensing [9] showed that germanium-on-silicon nitride waveguides can be used to measure the concentration of Isopropyl alcohol (IPA) in DI water, using a microfluidic channel. For a transmission wavelength of 3.73 μm and a waveguide loss of 7.9 dB/cm, the lowest measured concentration of IPA in acetone was 5% by volume for a 4 mm interaction length. The authors suggested that the limit of minimum volumetric concentration detection is dominated by the fluctuation of the laser input power, especially in a system whereby the analyte solution does not have high inherent absorption compared to the solvent.

Other works have shown the use of different platforms such as ZnSe deposited onto silicon waveguides with an interaction length of 3 mm [10]. The lowest concentration of IPA measured in water was 20% by volume. The guidance mechanism of the analyte was through a different approach in this paper, a filter paper strip was used rather than a microfluidic channel. Microfluidic channels can also be used for sample delivery, and they have the advantage of giving flexibility in sample treatment and delivery, since the channel can be reused after a simple cleaning process and does not have the issue of evaporation of the analyte. Furthermore, the microfluidic channels can be used to control the sample flow and pre-process the liquid samples before measurements are obtained. To attach the micro-fluidic channel to an SOI waveguide chip, a cladding layer needs to be deposited onto the sensing device, to act as a bonding layer. This cladding layer can also be used to ensure that there is no contact between the (potentially optically absorbing) microfluidic channel material and the sensitive waveguide surface, and to define where the sample interacts with the waveguide.

As a simple model to demonstrate absorption spectroscopy, an IPA/water mixture was chosen such that IPA acts as the analyte and water as the solvent. These were chosen as they are inexpensive and abundant materials, with well-characterized absorption spectra [9], [10].

Recently, we have shown that SOI waveguide can be used to measure water-IPA mixtures, with the smallest measured concentration being as low as 3% IPA in water (by volume).

Manuscript received October 14, 2021; accepted October 15, 2021. Date of publication October 19, 2021; date of current version November 11, 2021. This work was supported in part by the Engineering and Physical Sciences Research Council under Grants EP/L00044X/1, EP/L01162X/1 and EP/N00762X/1, in part by Royal Academy of Engineering under Grant RF201617/16/33, and in part by China Scholarship Council. *(Corresponding author; Yanli Qi.)*

Yanli Qi, Zhexuan Zheng, Yangbo Wu, Anushka Gangnaik, David J. Rowe, Vinita Mittal, Jonathan Butement, James S. Wilkinson, Goran Z. Mashanovich, and Milos Nedeljkovic are with the Optoelectronics Research Centre, University of Southampton, Southampton SO17 1BJ, U.K. (e-mail: yq1r17@soton.ac.uk; zz1f17@southamptonalumni.ac.uk; yw3a14@soton.ac.uk; a.gangnaik@soton.ac.uk; d.rowe@soton.ac.uk; v.mittal@soton.ac.uk; jb3006@orc.soton.ac.uk; jsw@ecs.soton.ac.uk; m.nedeljkovic@soton.ac.uk).

Mehdi Banakar is with the Zepler Institute for Photonics and Nanoelectronics, University of Southampton, Southampton SO17 1BJ, U.K. (e-mail: m.banakar@soton.ac.uk).

Data is available on-line at https://doi.org/10.5258/SOTON/D2014.

Digital Object Identifier 10.1109/JPHOT.2021.3121331

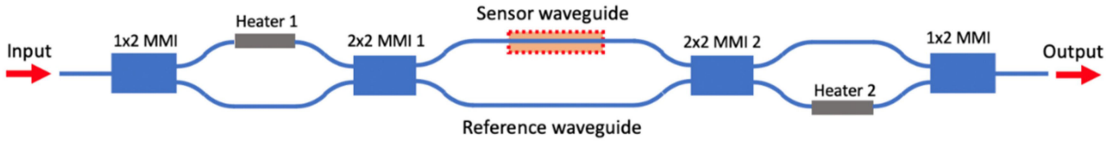

Fig. 1. Schematic diagram of the sensing circuit.

This was detected with a 500 μm interaction length with an integrated microfluidic channel [11]. The minimum detectable concentration (by volume) of this sensor was lower than in earlier works [9], [10].

However, an issue arose with the limit of sensitivity being restricted by the noise arising from both the experimental setup and environmental issues, such as the vibration of the input and output fibers. This occurs due to the reference and sample measurements occurring asynchronously.

To circumvent this problem, we have designed a novel silicon on insulator waveguide sensing circuit, with the insertion of thermo-optic switches before and after the sensing waveguide (see Fig. 1). This will allow for the ability to switch light continuously between a sensor arm and a reference arm. This would enable measurement of the transmission through a waveguide whose evanescent mode is exposed to a fluid analyte, immediately followed by a measurement of the transmission through a reference waveguide that is not exposed to the analyte. This would enable the removal of noise sources that would randomly affect the optical transmission through the chip, such as fluctuations of the laser source intensity, or variations in the coupling efficiency between the fibers and waveguides, which could either be caused by high frequency oscillations around a given setpoint, or by low frequency drift away from the setpoint.

In addition, the circuit can be used in combination with a lock-in amplifier for phase sensitive detection, which both helps with separating out the transmissions of the sensor and reference waveguides, and further reduces the measurement noise by removing detector noise at frequencies other than the frequency at which the light is being switched between the two waveguides, since the switching effectively encodes a constant frequency optical modulation onto the light wave.

A similar noise improvement could be achieved in an on-chip homodyne detection system in which light is split into a sensor waveguide and a reference waveguide, and waveguide integrated photodetectors placed at the end of each waveguide are used to measure the absorption by measuring the difference between the waveguide transmissions. Since the detectors are in fixed positions on the chip, this method would also remove noise coming from random fluctuations of the input light intensity. However, the major drawback is that integrating detectors with waveguides would dramatically increase fabrication complexity and cost, and is not currently possible at all mid-IR wavelengths. On the other hand, our proposed method achieves a similar result through the very simple (and much cheaper) addition of on-chip heaters. Only one external photodetector, potentially with higher performance than can currently be achieved in waveguide integrated photodetectors, is then required.

Considering the requirement for a low-loss waveguide platform, we used an SOI waveguide platform with a previously demonstrated low loss of 1.3 ± 0.7 dB/cm at 3.8 μm wavelength [12] to be the basis of the circuit. The SOI platform was chosen because it uses only standard fabrication processes, a library of well-optimized passive components is already available for the 3-4 μm wavelength range, and because silicon-on-insulator (SOI) technology can be accessed at low cost through multi-project wafer services in which near-infrared and MIR devices can be made on the same wafer. It is well known that IPA has signature absorption peaks in the wavelength range between 3.725 μm and 3.888 μm [13].

In this paper, we demonstrate the integration and operation of the switching sensor realized in the SOI platform with an integrated Polydimethylsiloxane (PDMS) microfluidic channel, and characterize its performance by using it to measure the absorption of water-IPA solutions at 3.77 μm wavelength. We investigate the noise of the absorption measurement, and show that the switch sensor is able to reduce noise by a factor of 11 compared to a simple waveguide absorption sensor.

II. Sensing Circuit and Measurement Scheme

Fig. 1 shows a diagram of the circuit (excluding grating couplers). The electric field output of the full device (E_{out}) can be calculated by multiplying the input electric field (E_{in}) with the S-matrix elements of each component in the full circuit (where the S-matrices describe the relationships between the electric fields at the input and output ports of each device):

$$E_{out} = S_{2x1MMI} \times S_{heater2} \times S_{2x2MMI2} \times S_{sensor} \times S_{2x2MMI1} \times S_{heater1} \times S_{1x2MMI} \times E_{in} \quad (1)$$

For simplicity, we (unrealistically) assume that there is no insertion loss in any of the multimode interferometers (MMIs) in this model, since any insertion loss would simply contribute to the insertion loss of the whole switch. For the 1x2 MMI we also assume that there is no imbalance or phase error (since the 1x2 MMI is inherently symmetrical if there are no significant fabrication defects):

$$S_{1x2MMI} = \frac{1}{\sqrt{2}} \begin{bmatrix} 1 \\ 1 \end{bmatrix} \quad (2)$$

For the 2x2 MMIs, we assume that there is an imbalance $B = P_{out1}/P_{out2}$, where P_{out1} and P_{out2} are the optical intensities at the two output ports, and the electric fields at the output ports are $E_{out1} \propto \sqrt{P_{out1}}$ and $E_{out2} \propto \sqrt{P_{out2}}$. We also assume that there is a phase error ξ between the two output ports. Then:

$$S_{2x2MMI} = \frac{1}{\sqrt{B+1}} \begin{bmatrix} \sqrt{B} & e^{j\left(\pi/2+\xi\right)} \\ e^{j\left(\pi/2+\xi\right)} & \sqrt{B} \end{bmatrix} \quad (3)$$

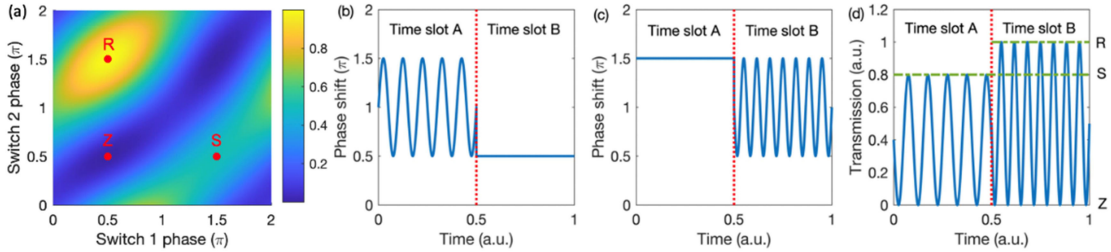

Fig. 2. (a) Map of transmission intensity for varying switch phase shifts, with "S" as the switch configuration for maximum transmission of the sensor arm, "R" as the configuration for maximum transmission of the reference arm, and "Z" as the configuration for least overall transmission. (b) and (c) show the phase shifts applied to the first and second switches respectively in each full time period. (d) shows the overall circuit transmission over a full time period. In (d) the time slot A and B signals are shown as having different amplitudes, representing the situation when there are different transmission intensities at the S and R points.

For the two waveguide arms in the switch Mach-Zehnder interferometer (MZI), where the waveguides are of the same length but a thermo-optic phase shifter in one arm has a phase change $\Delta\phi$ applied to it, we insert a phase error θ (but do not include an imbalanced loss in the two arms as the 2x2 MMI imbalance creates an equivalent effect):

$$S_{heater1} = \begin{bmatrix} e^{j(\Delta\phi + \theta)} & 0 \\ 0 & 1 \end{bmatrix} \tag{4}$$

$$S_{heater2} = \begin{bmatrix} 1 & 0 \\ 0 & e^{j(\Delta\phi + \theta)} \end{bmatrix} \tag{5}$$

In this experiment, the two heaters were placed in opposite arms of the two switches to simplify the layout design and experimental measurement, but they could be placed in either arm of the switch, in which case the S-matrices should be adjusted accordingly. In the sensor arm, the analyte introduces an absorption change $\Delta\alpha$ (in dB), with an accompanying transmission change $\Delta T = 10^{-\frac{\Delta\alpha}{10}}$ and an effective refractive index change Δn_{eff} that produces a phase change $\Delta\varphi$. The S-matrix for the sensor arm and reference arm combined in parallel (assuming no phase error or insertion loss in the reference arm) is then:

$$S_{sensor} = \begin{bmatrix} \sqrt{\Delta T} e^{j(\Delta\varphi)} & 0 \\ 0 & 1 \end{bmatrix} \tag{6}$$

Fig. 2(a) shows a map of the theoretically calculated transmission for all possible combinations of heater phase shifts, for an ideal circuit with no fabrication errors. Three points are marked on the map: 1. "S" $= (1.5\pi, 0.5\pi)$ –the combination of phase shifts needed to switch the light so that it passes into the sensor arm, and then light from the sensor arm is received by the output waveguide, i.e., the sensor arm transmission. 2. "R" $= (0.5\pi, 1.5\pi)$ – the phase shifts to switch light to the reference arm and to receive light from the reference arm, i.e., the reference arm transmission. 3. "Z" $= (0.5\pi, 0.5\pi)$ – the phase shift to switch light to the sensor arm but to receive it from the reference arm, i.e., a "zero" position where the transmission is minimized. The waveforms shown in Fig. 2(b) and (c) are applied to the two phase shifters so that in time slot A (equal to half of the measurement time) the light is modulated between the "S" and "Z" positions, and in time slot B the light is modulated between the "R" and "Z" positions.

The resulting relative optical transmission for the whole device takes the form shown in Fig. 2(d). The modulation in time slot A is applied at frequency f_A, while the modulation in time slot B is applied at frequency f_B. The sensor waveguide transmission S-Z is then retrieved by using a lock-in amplifier operating in dual reference mode to isolate the signal at frequency f_A, and the reference waveguide transmission R-Z at a different frequency f_B is simultaneously retrieved in the same way. The change in transmission due to the analyte is then found from the ratio (S-Z)/(R-Z). When using thermo-optic phase shifters the two frequencies f_A and f_B can be in the kHz regime so that the modulation frequency is higher than the frequency of many of the mechanical vibrations in our setup. The added benefit of using the lock-in amplifier in this detection scheme is that it would filter out much of the noise measured at the detector (e.g., random thermal noise) at frequencies other than at f_A or f_B.

SparaWe define the following variables for transmission through the device in four possible cases:

$\boldsymbol{I_S}$ = transmission intensity when the switches are configured for maximum transmission through the sensor arm, i.e., point "S";

$\boldsymbol{I_R}$ = transmission intensity when the switches are configured for maximum transmission through the reference arm, i.e., point "R";

$\boldsymbol{I_Z}$ = transmission intensity when the switches are configured for minimum overall transmission, i.e., point "Z";

$\boldsymbol{I_{S0}}$ = transmission intensity when the switches are configured for maximum transmission through the sensor arm, i.e., point "S", in the specific case when no analyte has been introduced to the sensor. This is effectively the background transmission.

We can additionally assume that there are likely to be different losses in the sensor and reference arms even when no analyte is introduced to the sensor arm (e.g., because of a different waveguide top cladding absorption in the sensing windows, or from losses at the point where there is a transition in the sensing arm between the silica top cladding and an air or liquid top cladding), such that:

$$I_{S0} = T_0 \, I_R \tag{7}$$

T_0 is the transmittance of the sensor arm when there is no analyte. In that case we can say that the transmittance of the

waveguide when an analyte is introduced is T_a, and that it can be calculated from:

$$T_a = \frac{I_S}{I_{S0}} = \frac{I_S}{T_0 I_R} \tag{8}$$

Random variations in the laser power or in the coupling efficiency to and from the chip would have the effect of multiplying the transmission intensities at all operating points in a particular instant by the same scaling factor N, so that

$$T_a = \frac{N I_S}{T_0 N I_R} = \frac{I_S}{T_0 I_R} \tag{9}$$

Thus these noise components can cancel out if the two absolute transmission intensities are measured simultaneously. In our approach the time between measurements is kept as small as possible, so as to remove lower frequency noise components like drift. However, if in our approach we continuously modulate between the points "S" and "Z" in time slot A and between "R" and "Z" in time slot B, and use a lock-in amplifier to measure the amplitude of the resulting optical signal in the two time slots, then we in fact measure the difference between the "S" and "Z" point and "R" and "Z" point transmission intensities, which we call M_S and M_R:

$$M_S = I_S - I_Z \tag{10}$$

$$M_R = I_R - I_Z \tag{11}$$

In a perfect MZI switch the value I_Z would be equal to zero, but in practice the MZI switches have finite extinction ratios, so that I_Z has a non-zero value. With the noise scaling factor N these become:

$$M_S = N(I_S - I_Z) \tag{12}$$

$$M_R = N(I_R - I_Z) \tag{13}$$

However, we can perform calibration measurements of the extinction ratios from the "S" and "R" positions compared to the "Z" position (ER_{S0} and ER_R), using a DC optical signal before an analyte is introduced, in order to partially compensate for the error coming from a finite extinction ratio.

$$ER_{S0} = \frac{I_Z}{I_{S0}} \tag{14}$$

$$ER_R = \frac{I_Z}{I_R} \tag{15}$$

Combining (12) and (14) together:

$$M_S = N(I_S - I_{SO} ER_{S0}) = N\left(I_S - \frac{I_S}{T_a} ER_{S0}\right) \tag{16}$$

$$I_S = \frac{M_S}{N\left(1 - \frac{ER_{S0}}{T_a}\right)} \tag{17}$$

And combining (13) and (15) together

$$M_R = N(I_R - I_R ER_R) \tag{18}$$

$$I_R = \frac{M_R}{N(1 - ER_R)} \tag{19}$$

From (8), (17), and (19):

$$T_a = \frac{I_S}{T_0 I_R} = \frac{\frac{M_S}{N\left(1 - \frac{ER_{S0}}{T_a}\right)}}{\frac{T_0 M_R}{N(1 - ER_R)}} \tag{20}$$

Finally, rearranging for T_a and substituting in (7), (14) and (15) we get:

$$\begin{aligned} T_a &= ER_{S0} + \frac{M_S}{T_0 M_R}(1 - ER_R) \\ &= ER_{S0} + \frac{ER_{SO} M_S}{ER_R M_R}(1 - ER_R) \end{aligned} \tag{21}$$

$$T_a\ (dB) = 10 log_{10}\left(ER_{S0} + \frac{ER_{SO} M_S}{ER_R M_R}(1 - ER_R)\right) \tag{22}$$

Alternatively, the absorption loss induced by introducing the analyte can be expressed as an absorption $A_a\ (dB) = -T_a(dB)$. In this final expression any multiplicative noise (such as that created by randomly varying optical coupling losses arising from fiber vibration) has been cancelled out, providing that the change in noise signal is much slower than the time between M_S and M_R measurements. Therefore, if we accurately measure ER_{S0} and ER_R before the analyte is introduced, and are able to "simultaneously" measure M_S and M_R in the presence of the analyte, then we can measure the analyte absorption A_a without multiplicative noise.

III. Theoretical Error Investigation

In this section we use the theoretical model described in the Section II to explore how design, fabrication, or calibration errors can affect the accuracy of the sensor region absorption measured using the device. We define the absorption error as:

$$\begin{aligned} &absorption\ error\ (\%) \\ &= 100 \times \left(\frac{measured\ sensor\ region\ absorption}{actual\ sensor\ region\ absorption} - 1\right) \\ &= 100 \times \left(\frac{A_a}{A} - 1\right) \end{aligned} \tag{23}$$

In this equation the actual absorption introduced by an analyte into the sensor region is A, and the measured sensor region absorption (from (22)) is A_a. We also define the variable A_0 to represent the absorption loss in the sensor region while the sensor is being calibrated with some reference substance present in the sensor region.

The phase errors in the switch arms (θ_1 and θ_2) and the phase shifter efficiencies can be calibrated and compensated for by measuring a 2D map of the overall switch transmission with varying powers applied to the two heaters, in order to find the heating powers required to set the device to the "S", "R", and "Z" positions. The remaining principal fabrication errors that would alter the device response are then the imbalances of the two 2× 2 MMIs (B_1 and B_2) and their phase errors (ξ_1 and ξ_2).

Fig. 3(a) shows a contour map of the absorption error for a range of imbalances and phase errors, with $B_1 = B_2$ and $\xi_1 = \xi_2$, when measuring an analyte with $A = 5$ dB, for the situation

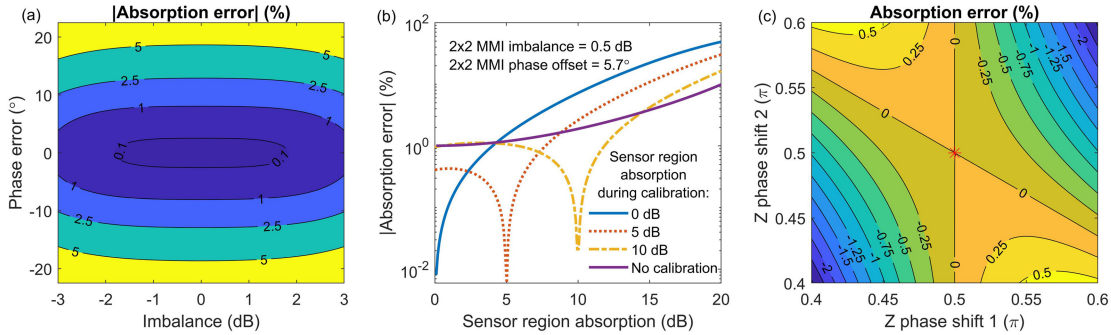

Fig. 3. Plots showing the theoretical percentage error in the measured analyte region absorption (compared to the actual analyte region absorption) in the presence of different fabrication or calibration errors: a) Contour map showing the error when different combinations of equal imbalances and phase errors are present in the two 2x2 MMIs. b) Line plot showing how the magnitude of the error varies for different actual sensor region absorptions, in the situation when the 2x2 MMIs each have an imbalance of 0.5 dB and phase offset of 5.7°. Three lines are shown that illustrate how the error vs. actual absorption relationship changes when switch calibration is performed using reference substances that yield different values of sensor region absorption. A fourth line shows the estimated error when the calibration is not performed, i.e., when the analyte absorption is calculated directly from M_S/M_R. (c) Contour map showing the error when the "Z" position is incorrectly calibrated, i.e., when the phase shifts applied using the heaters in the two switches are varied around the ideal "Z" position, 0.5π, 0.5π (which is marked on the figure with a red star). In (a) and (c) the sensor region absorption is set to 3 dB during calibration and 5 dB during measurement.

in which the calibration was carried out in the presence of a reference substance for which $A_0 = 3$ dB. From the contour map it can be seen that the error stays $< 1\%$ if the imbalance is within approximately $< \pm 3$ dB and the phase error $< 5°$, and also that this error can become very large for large imbalances and moderate phase errors.

Furthermore, the absorption error arising from the MMI phase error and imbalance depends strongly on the difference between the sensor region absorption during the measurement and during the calibration of the device extinction ratios ER_{SO} and ER_R. This is depicted in Fig. 3(b), which shows the magnitude of the absorption error when the sensing region absorption is varied between 0 dB and 20 dB, and when the calibration is performed at three different values of A_0. In each case the errors are dramatically smaller when the difference between the reference substance and analyte absorptions is small, implying that the calibration should be carried out using a reference substance whose absorption is as close as possible to the target analyte absorption. Fig. 3(b) also shows the calculated absorption error when no calibration is performed, which is to say, when the absorption is calculated directly from the ratio of M_S and M_R. We observe that performing the calibration can reduce the error by up to 2 orders of magnitude when the analyte absorption is close to the calibration absorption, but when the analyte absorption becomes much larger the calibration in fact introduces more error, and is therefore not necessary.

It can also be expected that inaccurate estimation of the phase shifter efficiencies and phase errors (θ_1 and θ_2) will lead to error in the measured absorption since the positions of "R", "S", and "Z" will be inaccurate. For simplicity we have estimated the absorption error when only one of these three measurement points is inaccurate at any one time, and found that absorption is most sensitive to the "Z" position. Fig. 3(c) shows the absorption error when the phase shift applied to each heater for the "Z" position is varied in the range 0.4-0.6π (with the ideal position being (0.5π, 0.5 π)). This calibration error on its own appears to result in smaller absorption errors than those arising from B and ξ. From Fig. 3(c) it is also clear that when Z phase shift 1 is 0.5π, then the absorption error does not appear to be affected by Z phase shift 2. When the Z phase shift 1 is 0.5π and there is no imbalance or phase error in the switch (as is the case in Fig. 3(c)), then the light is transmitted by the first switch entirely into the reference arm. The overall device transmission will still depend on the phase applied to switch 2, with the Z point transmission being at its lowest when Z phase shift is also 0.5π. However, the transmission will not depend on the sensor arm absorption, since the light does not pass through it. The consequence is that using ER_R and ER_{SO} during the calibration process will compensate for the Z transmission changing when Z phase shift 2 is not 0.5π, and the calculated absorption (and hence absorption error) will not be affected, so that in that situation the absorption is independent of Z phase shift 2.

Overall, these calculations suggest that great care should be taken to minimize the MMI imbalance and phase error during device design and fabrication, to accurately calibrate the thermo-optic phase shifters, and to perform the extinction ratio calibration with a background absorption close to the target analyte absorption. With typical fabrication and calibration errors the absolute error in the absorption measured using the device could be in the range of a few percent even before noise is considered.

IV. Waveguide Simulation and Switch Sensor Mask Design

Fig. 4 shows a cross-section of the SOI waveguide design, comprising a Si rib waveguide on a buried silicon dioxide (BOX) layer, with a 2 μm SiO_2 top cladding layer. Simulations in Lumerical MODE Solutions confirmed that a 2 μm cladding was thick enough to completely isolate the waveguide mode from an analyte. HF etching of the cladding layer is needed to produce a sensing window where the analyte is in contact with the waveguide. The partially-etched rib design ensures that the BOX layer is not affected by the HF etching of the cladding, as the 50 nm thick Si layer protects the BOX.

Lumerical MODE Simulations was used to simulate the absorption loss spectrum of an SOI waveguide with a top cladding

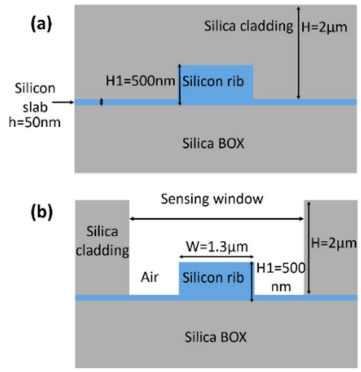

Fig. 4. 2D schematic of the SOI rib waveguide cross-section: (a) with silica cladding layer and (b) with an etched sensing window.

of pure IPA, using the wavelength-dependent refractive index, n, and extinction coefficient, k, of IPA [14], and the known parameters for Si and SiO_2. The model was constructed with a semi-infinite region of IPA above the waveguide. The absorption loss was simulated over a wavelength range from 3.725 μm to 3.888 μm. The resultant spectrum for TE polarization shows the absorption peak of pure IPA near 3.77 μm, with a peak wave-guide absorption of ∼130 dB/cm. Simulations confirmed that the TM polarization is not supported in the 500 nm SOI platform used in this work. In this case, the 1.8 mm interaction length was defined by etching windows through the cladding layer to test the sensitivity of the device to water-IPA solutions as a model solution.

V. Fabrication

For the fabrication process (Fig. 5), the SOI chips with 500 nm thick Si device layer (Fig. 5(a)) were patterned by electron-beam lithography, and 450 nm of Si was etched using an Oxford Instruments ICP 380 system by to create the rib waveguides (Fig. 5(b)). A 2 μm SiO_2 cladding layer was deposited on the top surface of the chips by Plasma Enhanced Chemical Vapour Deposition (PECVD) (Oxford Plasmalab System 100) (Fig. 5(c)), then the sensing windows were opened by isotropic HF wet etching (Fig. 5(d)). To create the sensing windows, a 2 μm thick layer of PMMA photoresist was spun on to the wafer, and was subsequently e-beam patterned. Liquid hydrofluoric acid (HF) was used to remove 2 μm SiO_2 in order to open sensing windows, with 20:1 ratio of DI water:HF. HF selectively etches SiO_2 but not Si in regions where the photoresist is not present. The wafer is then placed in NMP at 50°C for 20 minutes to remove the PMMA. The isotropic HF wet etching will cause the width at the bottom of the sensing window to be slightly narrower than at the top of the sensing window.

Fig. 5(e) shows a spiral waveguide with a sensing window. The spiral waveguide is used for a longer interaction length while maintaining a small footprint. The lighter regions are the open sensing areas, while the darker regions are those covered by the SiO_2 cladding layer. 150 nm of aluminum was deposited on the surface of the SiO_2 for the heaters (Fig. 5(f)). In this case, PDMS was used to fabricate the microfluidic channel to be bonded onto the surface of the SiO_2 cladding layer, because mature fabrication techniques are already available for this material [15]. For the PDMS fabrication process: A clean petri dish was prepared to contain the PDMS materials which are Sylgard 184 base and agent with 10:1 ratio (Sylgard 184 base: agent) [16]. They then were mixed together and the mixture was poured into the mould. The mould was created by 3D printer. The filled mould was put into a vacuum chamber for at least 30 minutes until no bubbles were left in the mixture. The mould and mixture were then placed into an oven at 150 degrees for 10 mins to cure the PDMS. After curing the microfluidic channel, a 1mm Miltex Biopsy punch with a plunger was used to make holes through the channel (Fig. 5(g)), so that tubes could be inserted. The sensing window area was covered by a microfluidic channel which was 3 mm wide (w), 0.5 mm high and 20 mm long (L) (Fig. 5(g)).

A plasma Asher (PVA TEPLA 300 AL) was used to heat the SiO_2 and Sylgard 184 in an O_2 environment to cause covalent bonding between the two surfaces. (Gas flow rate: 1052 ml/min of O_2, power of 30 W, time: 31 seconds). The result is shown in Fig. 5(h). Although PDMS has high mid-infrared absorption, the silica top cladding prevents the light from interacting with the PDMS [17]. A plasma asher was used to heat the silica and PDMS in an O_2 environment to cause covalent bonding between the two surfaces.

VI. Measurements

The experimental system is set up so that light can be coupled through the photonic circuit, and electrical signals can be applied to the two heaters through the use of electrical probes. The probes are held in place by clamps, and make physical contact with the heaters. A liquid sample can be pumped through the microfluidic channel by a syringe pump. Fig. 6 shows a diagram of the setup.

Fig. 7 shows a photograph of the experimental measurement setup. The light source was a tunable QCL laser (3.725-3.888 μm) (Daylight Solutions) [18] and the light was coupled into a fluoride fiber (P3-32F-FC-2 from Thorlabs) by a ZnSe lens, and then from the fiber into the waveguides using surface grating couplers. A pair of electrical probes were positioned on top of on-chip metal contact pads connected to each of the two heaters, using 3-axis micropositioners built into the probe bases. At the output end of the photonic circuit, light was coupled to the output MIR fiber and subsequently to the MIR detector (IS-1.0 InSb detector, InfraRed Associates Inc). A syringe pump forced the fluid sample through the microfluidic channel via input and output tubes. The chip (dimensions: 36mm × 27mm) was kept still during measurements using a vacuum stage.

A. Sensor Calibration Measurements

Before the sensor can be used, a calibration step is carried out to find the correct driving voltages for the two heaters (see Fig. 1), to find the efficiency and phase offsets of the switches. The laser is set at 3.77 μm wavelength, because IPA has a signature absorption peak at 3.77 μm. During the calibration a dual output signal generator is used to apply a DC electrical signal to the probes, then the optical chopper is switched on, and the lock-in amplifier is used in single channel mode to retrieve the amplitude of the modulated optical signal. The voltage applied across each heater is swept (0-2.35V) and at each voltage combination the electrical currents and optical transmission are recorded. Electrical power

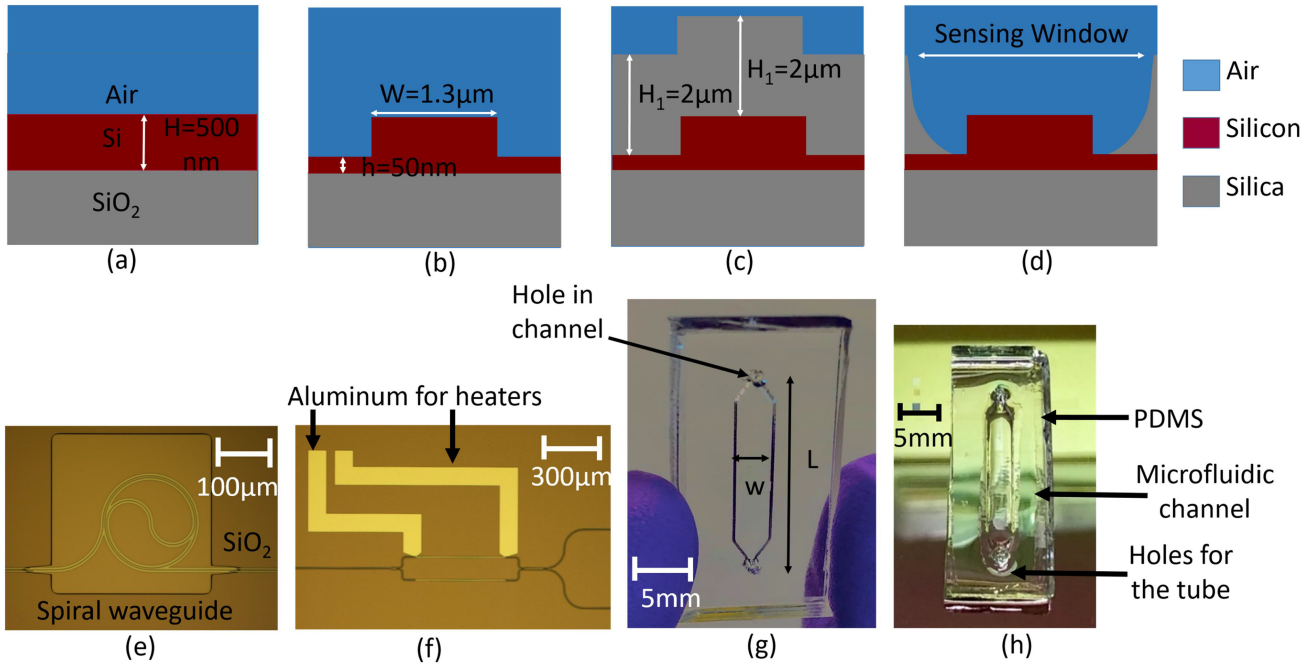

Fig. 5. Fabrication process of SOI waveguide chip with bonded PDMS microfluidics channel. (a–d) show diagrams of the fabrication process, (e) shows an optical microscope image of a fabricated spiral waveguide in the sensing window, (f) shows a microscope image of a fabricated MZI switch. (g-h) display photographs of the PDMS channel with (g) showing the dimensions of the design and (h) highlighting the aspects of the design.

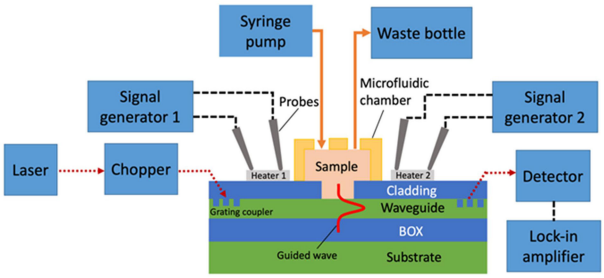

Fig. 6. Diagram of the system layout.

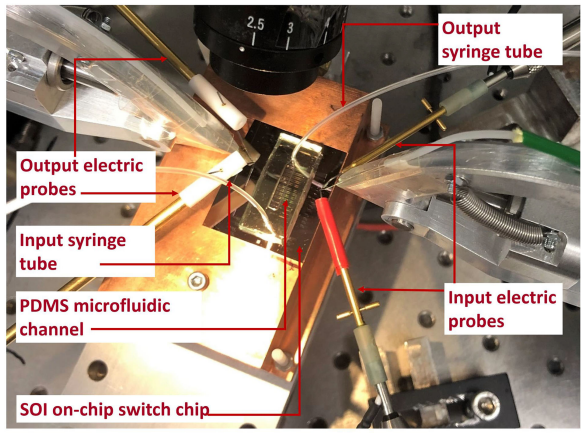

Fig. 7. A photograph of the experimental apparatus for testing the sensor with a syringe pump, sample in the syringe, input tube, input fiber, output fiber, output tube, and electrical probes.

applied was calculated from the voltage and measured current through the heater, and then used to produce a transmission map like the one in Fig. 2(a). Water is then flowed through the microfluidic channel, and the measurement is then repeated, and the difference in optical transmission is analysed. The "S" position is then determined by finding the power combination with maximum change in transmission (0.2761 W, 0.2761 W), "Z" is a point at which the transmission is low in both cases and there is very little change in transmission (0.2761 W, 0.0020 W), and "R" is a point when there is high transmission in both cases and there is the minimum change in transmission (0.0814 W, 0.0814 W). ER_{SO} and ER_R are calculated based on the measured DC transmissions at these three operating points.

After finding the driving voltages of the MZI switches required to tune to the "S", "R", and "Z" operating points, a signal generator supplies waveforms with the shapes shown in Fig. 2(b) and (c) to the thermo-optic phase shifters, where the voltages are chosen to correspond to the three operating points. The waveform is set up so that in time slot A the frequency is $f_A = 6$ kHz (see Fig. 2(b)) and in time slot B the frequency is $f_B = 7$ kHz (see Fig. 2(c)). The lock-in amplifier is then switched to dual channel mode so that it retrieves the amplitudes of the optical transmissions at these two frequencies, where one corresponds to the measurement M_S and the other to the measurement M_R.

B. Time Series Measurements and Stability Performance of the Switch Sensor

Allan deviation measurement can be used as a method for analyzing the noise and stability of the switch sensor [19].

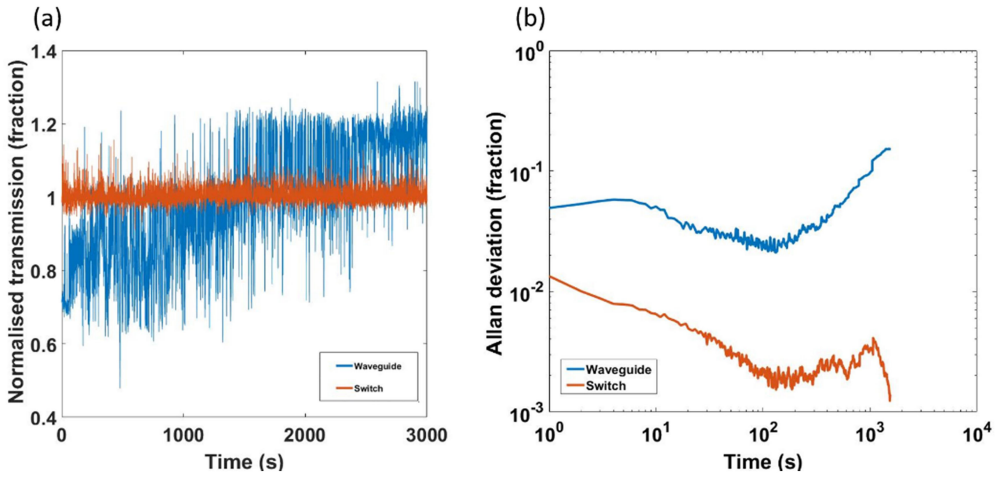

Fig. 8. (a) Time series of the normalized transmissions of the switch sensor and waveguide sensor, (b) Allan deviation of the time series.

To compare the stability of the switch sensor and a simple waveguide sensor without the switch circuit, we measured a time series of the transmission of a straight waveguide over 47 minutes, as well as a time series of the extracted transmittance of the sensing region of the switch sensor for the same length of time, both without an analyte present in the sensing region. Both time series were normalized to their mean values, and are plotted in Fig. 8(a). During the measurement the time constant of the lock-in amplifier was set to 5s.

As Fig. 8(a) shows, qualitatively the normalized transmittance of the switch sensor (orange colour line) is flatter than that of the waveguide sensor (blue colour line), both in terms of high frequency fluctuations and in terms of long-term drift. The Allan deviation is a quantitative measure of the average deviation of the signal over varying time periods and is shown for both sets of time series data in Fig. 8(b). It is evident that for all time periods the deviation of the switch sensor is lower than for the waveguide sensor. The smallest Allan deviations achieved by the waveguide and switch are 2.1% and 0.2% respectively, showing that the switch sensor can reduce the measured noise by a factor of as much as 11 times.

Furthermore, from the Allan deviation results, for the waveguide sensor it can be seen that initially as the averaging time is increased to 10s the deviation slightly increases, before reducing until just over 100s, when the deviation reaches a minimum. Beyond approximately 200s the deviation increases, showing that drift of the signal becomes dominant, and preventing further noise reduction by averaging. On the other hand, for the switch sensor as the averaging time increases the deviation immediately decreases with a faster slope than the waveguide sensor until approximately 200s, before also becoming dominated by drift for longer periods. This data shows that not only does the switch circuit reduce noise in the measured sensor transmittance, but it is also less susceptible to drift, which allows averaging to be used to even further reduce the noise.

Further measurements of the laser emission stability and detector noise floor make it clear that the simple waveguide noise and drift is predominantly caused by variation of the input and output fiber positions, affecting the fiber-waveguide coupling efficiency. However, where does the remaining noise in the switch sensor measurement come from?

We took time series measurements of the currents passing through each of the switch heaters at constant voltage, and found that for one of the heaters over 1000 seconds the standard deviation of the current measurements reached 1.0% and exhibited significant drift, due to movement of the electrical probes connected to the heater. Effectively this noise would manifest as a noise in the S, R, and Z positions during the measurement, leading to varying errors in the absorption measurement. In a future experiment the susceptibility of the switch sensor to this noise source could be lessened by using a more mechanically stable method to electrically contact the heaters, for example by creating wire bonds between the heater contact pads and a driving PCB.

Furthermore, the drift of the mechanical positions of the electrical probes meant that while performing the experiments, sometimes the voltages found to reach the S, R, and Z positions during calibration would no longer be valid by the time the analyte measurement was performed, leading to inaccuracy in the calibration. Solving the mechanical issues would help to solve this issue too.

Beyond this, some of the remaining noise will come from the incorrect earlier assumption that the measurements of the transmissions through the sensor and reference waveguide are occurring simultaneously, when in fact there is a small time offset between the measurements, so that the common noise components do not cancel perfectly. The ultimate limit of the noise rejection improvement that can be achieved using this sensing scheme without the presence of significant electrical noise should be investigated in future work.

C. *Sensing Demonstration*

After characterizing the noise properties of the sensor without an analyte, we tested whether the switch is able to correctly measure the absorption of an analyte, whilst at the same time

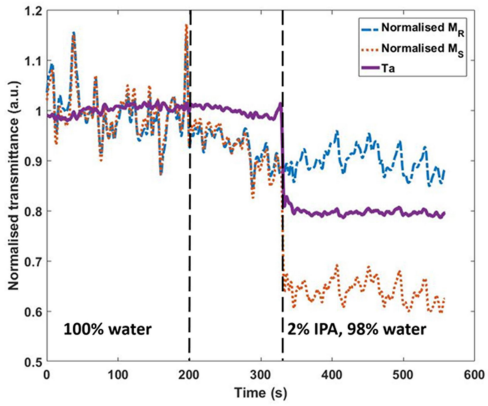

Fig. 9. Time series measurement of transmission through the sensor arm (orange), the reference arm (blue), and the corrected relative transmittance of the analyte (purple) where each signal is simultaneously retrieved by the lock-in amplifier. The transmission in each arm is normalized to the mean of the water only transmission in that arm during this time series.

reducing the noise of the measurement. We measured M_S, M_R, and T_a using the switch over a period of 555 seconds with data points recorded every 0.2 seconds, and with the lock-in amplifier time constant set to 5 s.

There were 3 stages in this measurement. In the first stage (0-200 s) there was DI water present in the microfluidic channel. From 200-330 s, a mixture of 2% IPA (by volume) and 98% DI water was pumped through the input tube until the mixture filled the microfluidic channel. Pumping of the sample was then stopped, so that the mixture remains in the microfluidic channel throughout the third stage (330-555 s). The data are plotted together in Fig. 9, each normalized to their mean values in the first period (where only water was in the sensing channel), so that their fractional changes can be directly compared.

Initially, when only DI water flows through the microfluidic channel, the transmission of the reference arm, sensor arm, and corrected relative transmittance each have a value close to 1. The transmissions of the reference arm and sensor arm follow very similar patterns to each other, but are also quite noisy. However, the corrected sensor transmittance (purple line) is clearly less noisy than the transmissions of the reference arm and sensor arms. This would be expected, since the M_S and M_R measurements would include similar noise in the optical input power to the switch, whereas that noise should largely be filtered from the T_a measurement. A simple waveguide sensor of the type in [11] could be expected to have the same noise level as seen in the M_S and M_R measurements, since it would be equally susceptible to the optical input noise.

After approximately 330 seconds an IPA/water mixture flows through the device. A change in the transmission is seen for the sensing arm, because it interacts with the IPA/water solution, whereas the reference arm transmission remains unchanged. The value of the corrected sensor transmittance also changed at the same time as the transmission of the sensing arm, corresponding to a change in the absorption of the sample at 3.77 μm wavelength with 1.8mm interaction length of 0.99 dB. In [11] a similar waveguide sensor was measured to have an absorption of 0.16 dB for a length of 500 μm for a 2% IPA concentration in DI water. Using the Beer-Lambert law, the same sample would be expected to have an absorption of 0.57 dB for a 1.8 mm interaction length, which is 40% lower than measured using the switch sensor. The discrepancy could be caused by fabrication errors in the sensor region length or the waveguide dimensions in either experiment, causing an error in the assumed effective optical interaction length. However, the absorption measured by the switch sensor may indeed include an error in the absolute value of the absorption measured by the switch sensor that could be the result of calibrating the switch sensor to incorrect S, R, and Z points. Such an error could be compensated for in an experimental setting by simply calibrating the sensor absorption using a sample with a known absorption value.

The root mean square (r.m.s) noise of the T_a measurement before 200 s is 0.9%, and after 330 s it is 1.3% of the normalized value, whereas for M_S it is 5.9% and 3.6% respectively, showing that the switch reduced the noise by a factor of 7 before 200 s and by a factor of 3 after 200 s in this measurement.

VII. Conclusion and Future Work

An SOI circuit with integrated thermo-optic switches and microfluidic channel has been demonstrated for use as a mid-infrared absorption sensor with reduced noise compared to a simple waveguide absorption sensor. The circuit works by alternately measuring the relative sensor channel and reference channel transmissions, from which a change in absorption due to a liquid analyte can be observed. A calibration and measurement scheme for using the device was proposed, and it was demonstrated by using it to measure the difference in absorption between 100% DI water and a solution of 2% IPA in 98% DI water. The results show that the switch sensor is able to lower the noise floor by a factor of 11 compared to a simple waveguide sensor, which would ultimately allow the switch sensor to measure lower concentrations of a target analyte, to reach a lower limit of detection.

However, we believe that the performance of the device can be improved by increasing the mechanical stability of the electrical contacts, for example by wire bonding electrical connections onto the chip, in order to reduce noise in the electrical signal driving the thermo-optic switches. This would improve both the noise rejection of the device and the absolute accuracy of the absorption measurement. The absolute accuracy of the absorption measurements could also be improved by first carrying out a calibration measurement of a sample with known optical absorption at the wavelength of interest.

Beyond this, methods such as liquid-liquid extraction could be used prior to MIR characterization to remove the analyte to a solvent with lower absorption. For example, most organic solvents have lower MIR absorption than water so extraction would allow a lower limit of detection when the sample is characterized using the waveguide sensor [20]. This is particularly relevant to clinical analysis as biological samples are typically aqueous. In summary, a detection of 2% IPA in water was achieved with an interaction length of 1.8 mm SOI chip integrated with a microfluidic channel and operating in the 3.77 μm wavelength.

REFERENCES

[1] L. Wang and B. Mizaikoff, "Application of multivariate data-analysis techniques to biomedical diagnostics based on mid-infrared spectroscopy," *Anal. bioanalytical Chem.*, vol. 391, no. 5, pp. 1641–1654, 2008.

[2] B. Sun *et al.*, "Mid-infrared quartz-enhanced photoacoustic sensor for ppb-Level CO detection in a SF6 gas matrix exploiting a T-Grooved quartz tuning fork," *Anal. Chem.*, vol. 92, no. 20, pp. 13922–13929, 2020.

[3] G. Giubileo and A. Puiu, "Photoacoustic spectroscopy of standard explosives in the MIR region," *Nucl. Instruments Methods Phys. Res. Sect. A: Accelerators, Spectrometers, Detectors Assoc. Equip.*, vol. 623, no. 2, pp. 771–777, 2010.

[4] C. Wang and S. Peeyush, "Breath analysis using laser spectroscopic techniques: Breath biomarkers, spectral fingerprints, and detection limits," *Sensors*, vol. 9, no. 10, pp. 8230–8262, 2009.

[5] A. Ergin, R. Greene, and G. A. Thomas, "Spectroscopic distinguishability of glucose from tissues in the porcine eye," in *Proc. IEEE 30th Annu. Northeast Bioeng. Conf.*, Springfield, MA, USA, 2004, pp. 233–234.

[6] S. Paul, M. R. McAinsh, and F. L. Martin, "Biospectroscopy for plant and crop science," *Comprehensive Anal. Chem.*, vol. 80, pp. 15–49, 2018.

[7] M. S. H. Akash and K. Rehman, "Infrared spectroscopy," in *Essentials of Pharmaceutical, Analysis.*, Singapore: Springer, pp. 57–80, 2020.

[8] S. Markus, J. Haas, P. Michler, M. Godejohann, and B. Mizaikoff, "Mid-infrared spectroscopy platform based on GaAs/AlGaAs thin-film waveguides and quantum cascade lasers," *Anal. Chem.*, vol. 88, no. 5, pp. 2558–2562, 2016.

[9] W. Li *et al.*, "Spiral waveguides on germanium-on-silicon nitride platform for mid-IR sensing applications," *IEEE Photon. J.*, vol. 10, no. 3, Jun. 2018, Art. no. 2201107.

[10] V. Mittal, M. Nedeljkovic, D. J. Rowe, G. S. Murugan, and J. S. Wilkinson, "Chalcogenide glass waveguides with paper-based fluidics for mid-infrared absorption spectroscopy," *Opt. Lett.*, vol. 43, no. 12, pp. 2913–2916, 2018.

[11] Y. Qi *et al.*, "Integration of mid-infrared SOI photonics with microfluidics," *Silicon Photon. XIV*, vol. 10923, 2019, Art. no. 109230I.

[12] G. Z. Mashanovich *et al.*, "Silicon photonic waveguides and devices for near-and mid-IR applications," *IEEE J. Sel. Topics Quantum Electron.*, vol. 21, no. 4, pp. 407–418, Jul./Aug. 2015.

[13] A. Kramida, Y. Ralchenko, J. Reader, and NIST ASD Team, "NIST atomic spectra database (version 5.8)," National Institute of Standards and Technology, Gaithersburg, MD. Oct. 2021. [Online]. Available: https://physics.nist.gov/asd

[14] E. Sani and A. Dell.'Oro., "Spectral optical constants of ethanol and isopropanol from ultraviolet to far infrared," *Opt. Mater.*, vol. 60, pp. 137–141, 2016.

[15] G. M. Whitesides, "The origins and the future of microfluidics," *Nature*, vol. 442, no. 7101, 2006, Art. no. 368.

[16] O. Ojuroye, R. Torah, and S. Beeby, "Modified PDMS packaging of sensory e-textile circuit microsystems for improved robustness with washing," *Microsystem Technol.*, vol. 18, pp. 1–8, 2019.

[17] Z. Han1 *et al.*, "On-chip mid-infrared gas detection using chalcogenide glass waveguide," *Appl. Phys. Lett.*, vol. 108, no. 14, pp. 141106, 2016.

[18] M. Nedeljkovic *et al.*, "Silicon photonic devices and platforms for the mid-infrared," *Opt. Mater. Exp.*, vol. 3, no. 9, pp. 1205–1214, 2013.

[19] E. Naser, H. Hou, and X. Niu, "Analysis and modeling of inertial sensors using allan variance," *IEEE Trans. Instrum. Meas.*, vol. 57, no. 1, pp. 140–149, Jan. 2009.

[20] K. Robert, C. Fleischer, F. Lanza, K. Boos, B. Sellergren, and D. Barceló, "Evaluation of a multidimensional solid-phase extraction platform for highly selective on-line cleanup and high-throughput LC− MS analysis of triazines in river water samples using molecularly imprinted polymers," *Anal. Chem.*, vol. 73, no. 11 pp. 2437–2444, 2001.